GMR
The Original

# GREEN SYNTHESIS OF PHASE-CONTROLLED A- AND B-$MNO_2$ NANOSTRUCTURES: STRUCTURAL, OPTICAL, AND ANTIMICROBIAL PROPERTIES FOR BIOMEDICAL APPLICATIONS

**Naila Raziq[1]*, Ambrin Akhtar[2], Ayesha Siddiqa[3], Efrah Mansoor[4]. Ezza Mansoor[5], Emaan Mansoor[6], Afsheen Mansoor[7], Sudhair Abbas Bangash[8]**

[1]Faculty of Life Sciences, Department of Pharmacy, Sarhad University of Science and Information Technology, Peshawar, Pakistan Email: naila.fls@suit.edu.pk
[2]School of Chemistry and Chemical Engineering, Shanxi University, Taiyuan, Shanxi, China, Email: akhtarambrin@sxu.edu.cn
[3]Institute of Microbiology and Molecular Genetics, University of the Punjab, Lahore, Pakistan, Email: ayesha.mmg@pu.edu.pk
[4]Islamic International Dental College, Riphah International University, Islamabad, Pakistan, Email: eframansoor2@gmail.com
[5]Islamic International Dental College, Riphah International University, Islamabad, Pakistan, Email: ezzamansoor1@gmail.com
[6]Islamic International Dental College, Riphah International University, Islamabad, Pakistan, Email: emaanmansoor5@gmail.com
[7]Department of Dental Material Sciences, Shaheed Zulfiqar Ali Bhutto Medical University, Islamabad, Pakistan,
Email: drafsheenqamar@gmail.com
[8]Faculty of Life Sciences, Department of Pharmacy, Sarhad University of Science and Information Technology, Peshawar, Pakistan,
Email: sudhair.fls@suit.edu.pk
*Corresponding Author: Sudhair Abbas Bangash, Email: sudhair.fls@suit.edu.pk

## ABSTRACT

In the work, preparation of α- and β-phase manganese dioxide ($MnO_2$) nanostructures was done in an eco-friendly route through a green synthesis method. X-ray diffraction (XRD), scanning electron microscopy (SEM), energy-dispersive X-ray spectroscopy (EDS), fourier transform infrared spectroscopy (FTIR), and UV-visible spectroscopy were used in a systematic way to characterize the synthesized materials. XRD analysis revealed the successful formation of crystalline α-$MnO_2$ and β- $MnO_2$ with different structural features. SEM micrographs showed that α-MnO2 had a nanowire-like morphology, but β-MnO2 had nanosheet-like morphologies, implying morphology-dependent phase growth in the presence of green synthesis. The presence of manganese and oxygen without major impurities as confirmed by the EDS results confirmed the purity of the synthesized samples. The FTIR spectra showed typical $MnO_2$ vibrational modes which further confirmed the formation of Mn-O phases. The optical absorption behaviours evaluated by UV–visible tests revealed significant optical absorption characteristics of the nanostructured materials, which imply their applicability in photonic and biomedical applications. Both phases were tested against the chosen microbial strains regarding their antibacterial and antifungal effects, with β-$MnO_2$ showing much higher antimicrobial activity than that of α-$MnO_2$. The better bioactivity of β -$MnO_2$ is explained by the increased surface area and the nanosheet structure which enables the increased interaction with microbial cells. In sum, green synthesis route offers a viable approach to the synthesis of phase-controlled $MnO_2$ nanostructures that have potential biomedical applications.

## 1. INTRODUCTION

The emergence and rapid dissemination of antimicrobial resistance (AMR) have become one of the urgent issues in contemporary medicine and health care. Bacterial and fungal diseases, which have been readily treatable by medicines, are becoming hard to manage as a result of the adaptive nature of microorganisms [1]. The pathogens like the multidrug resistant bacteria and opportunistic fungi have evolved complex defense systems and these are enzymatic degradation of drugs, alteration of drug targets, activation of efflux pumps and formation of biofilms. The adaptations greatly diminish the efficacy of traditional antibiotics and antifungal drugs [2]. Meanwhile, the pipeline of new antimicrobial drugs is also rather small, in part because this process is very expensive, time-consuming, and resistance develops to newly introduced compounds faster. Such a situation of increasing resistance and a slow-paced drug discovery indicates the pressing necessity of new innovative and sustainable approaches to antimicrobial strategies[3]. Besides resistance, conventional antimicrobial agents usually pose various limitations, such as being toxic to human cells, inability to survive in physiological conditions, and limited activity spectrum [4]. Fungal infections especially are very dangerous to immunocompromised patients and the existing antifungal treatments are often linked with side effects and resistance problems. Also, the development of microbial biofilms makes it even more difficult to treat, because biofilms create protective shields that do not allow penetration of drugs and increase the survival of microbes. All these issues characterize the main issue of the current study: the necessity to create effective, broad-spectrum, and

resistance-resistant antimicrobial materials, which could overcome shortcomings of conventional treatments [5]. Nanotechnology has become an appealing area of research in combating antimicrobial resistance, where materials possessing distinct physicochemical characteristics are available that are very different to bulk materials. Metal oxides are one of the nanomaterials that have attracted much attention because of their stability, biocompatibility, and good antimicrobial potential [6]. The manganese dioxide ($MnO_2$), specifically has been proposed as a very promising candidate because of its great redox characteristics, catalytic behavior and capacity to interact with biological systems at the nanoscale. Its general applicability, affordability, and environmental friendliness also contribute to its attractiveness as an antimicrobial agent. The antimicrobial effect of $MnO_2$ can be explained by a cascade of interrelated events which eventually results in inactivation of microbes [7]. To begin with, $MnO_2$ nanoparticles are first contacted with microbial cells by electrostatic interactions. The surfaces of most bacterial and fungal cells have an overall negative charge and $MnO_2$ nanoparticles may have adhesive surface characteristics. This very proximity is important, with $MnO_2$ having a direct action on the cell membrane. $MnO_2$ interferes with cell membrane integrity disrupting cell membrane permeability upon attachment[8]. This rupture results in leakage of vital components of the cell like ions, proteins and nucleic acid thus compromising the viability of the cell. After the interaction of membranes $MnO_2$ is an important molecule in the formation of reactive oxygen species (ROS). $MnO_2$ is a redox-active material, which may catalyze reactions involving the generation of highly reactive species, including hydroxyl radicals (OH), superoxide anions ($O_2$-), and hydrogen peroxide ($H_2O_2$ ). These ROS can cause oxidative stress in the cells of the microbes [9]. Oxidative stress leads to destruction of important cellular elements, such as lipid peroxidation in membranes, protein denaturation, and DNA fragmentation. Such extent of damage interferes with the normal functions of cells and does not allow them to replicate. Besides the process of ROS generation, $MnO_2$ has the ability to disrupt the metabolic processes in the microbes. It may bind with respiratory and energy-generating enzymes, and interfere with the electron transport chain, decreasing ATP generation [10]. This interference with metabolism further inhibits the survival of the microorganism. $MnO_2$ can also influence in fungal cells the cell wall synthesis and integrity, which is vital in maintenance of fungal structure and functionality. The next significant feature of $MnO_2$ activity is that it may prevent the formation of biofilms. $MnO_2$ can prevent biofilm formation and maturation by interfering with initial cell adhesion and causing oxidative stress. This is especially important since biofilms are very much recalcitrant to traditional antimicrobial therapy and are one of the primary causes of infections that are persistent in nature [11, 12]. The net outcome of these processes is membrane disruption, induction of oxidative stress, interference with metabolism, and biofilm inhibition leading to effective antibacterial and antifungal action. Noteworthy, the multi-targeted mode of action of $MnO_2$ inhibits the probability of microorganisms developing resistance, since it would need the development to co-adapt to several harmful pathways [13]. In this work $MnO_2$ is prepared using green synthesis and it is systematically explored with its antibacterial and antifungal applications, with a view to coming up with an effective and consistent material in treating microbial infections.

**Green synthesis of $MnO_2$**

A green synthesis of manganese dioxide ($MnO_2$) nanoparticles was done by a plant-mediated method, where the aqueous plant extract was used as a reducing and stabilizing agent as illustrated in figure 1. The leaves of fresh plants were well rinsed in distilled water to eliminate dust and contaminants and dried at room temperature. The washed leaves were then cut into fine pieces and the plant extract was obtained by boiling the leaves in deionized water at 60-80 C between 20-30 min. The mixture that arose was cooled to room temperature and filtered with Whatman filter paper to eliminate solid remnants resulting in the creation of a clear extract which was stored at 4 o C until further use. To prepare $MnO_2$, a potassium permanganate ($KMnO_4$) aqueous solution of the right concentration (usually 0.01 0.1 M) was prepared. $KMnO_4$ solution at room temperature was stirred constantly and drop-by-drop with the plant extract. The reaction was stirred 1-3 h during which the change of the color of the reaction mixture was gradually changing deep purple to brown or black, which was the indication of the decrease in the amount of permanganate ions (Mn) to manganese dioxide ($MnO_4$ ). Phytochemicals contained in the plant extract e.g. phenols and flavonoids enhanced the reduction process and they also served as capping agents to stabilize the formed nanoparticles. The pH of the reaction mixture was kept track of and dilute NaOH or HCl solutions used to adjust the pH, where pH is also important in regulating the morphology and size of synthesized $MnO_2$. The reaction temperature was also altered to 25, 40 and 80 o C in order to investigate the impact of temperature on the formation of particles and crystallinity. The mixture was left to settle after the reaction was complete and the precipitate was centrifuged at 6000-10,000 rpm over 10-15 min. To eliminate any unreacted precursors and organic compounds, the precipitate obtained was washed in distilled water and ethanol a couple of times. A hot air oven at 6080 ºC was used to dry the purified product followed by 1224 h to get fine powder of $MnO_2$ nanoparticles. In others, additional calcination was done at moderate temperatures (200-400 ºC) to enhance crystallinity and eliminate any residual organic matter.

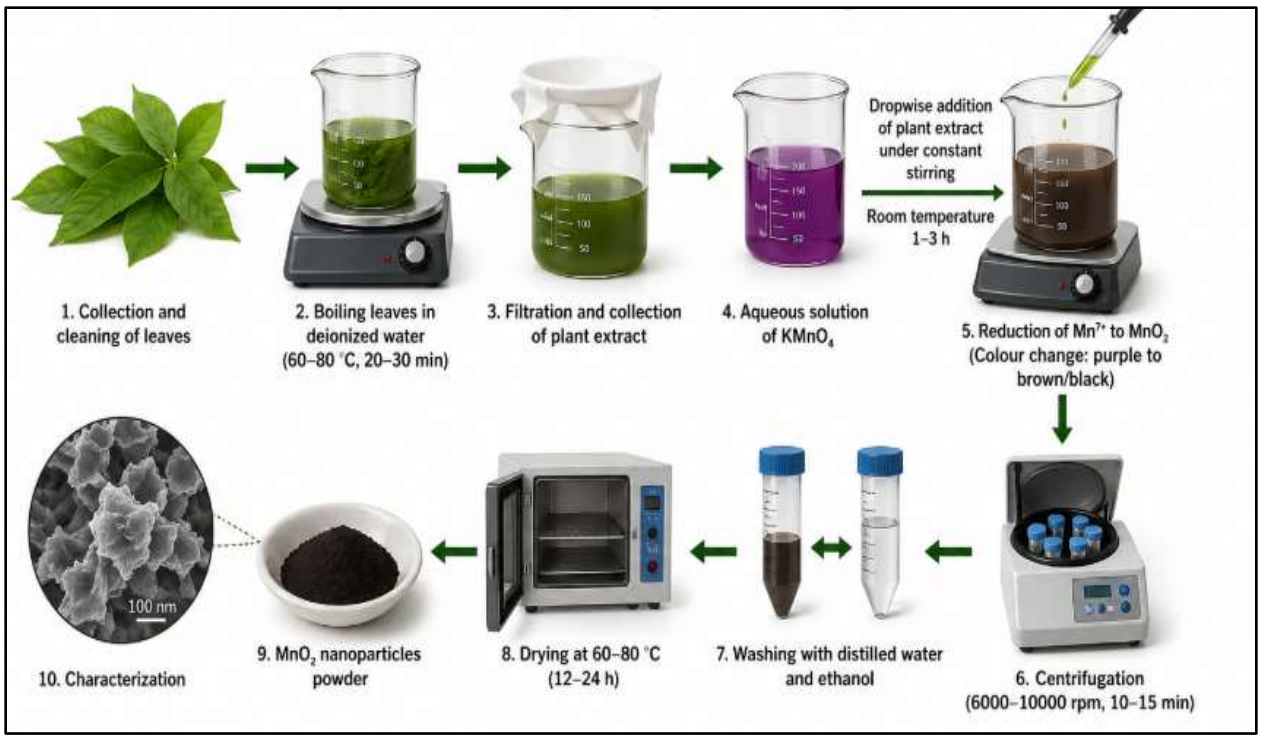


Figure 1: Green synthesis of $MnO_2$ nanoparticles using plant extract, illustrating the stepwise eco-friendly process from leaf collection and extract preparation to reduction of potassium permanganate ($KMnO_4$), formation of $MnO_2$ nanoparticles, purification, and final characterization under mild and sustainable reaction conditions.

## 2. RESULTS AND DISCUSSION

### 2.1 XRD

The X-ray diffraction (XRD) patterns shown in the figure 2 give a good comparative study of the α- and β-phases of $MnO_2$, denoted by the blue and red curves, respectively. The blue diffraction pattern is associated with α-$MnO_2$ and is in agreement with the standard data of the JCPDS card no. 44-0141, which indicated a tetragonal hollandite-type structure was formed. The characteristic diffraction peaks observed at 2θ values of approximately 12.7°, 18.0°, 28.7°, 37.4°, 49.8°, and 60.2° are indexed to the (110), (200), (310), (211), (411), and (521) crystallographic planes, respectively [14]. The existence of comparatively wide peaks indicates a reduced crystallinity and a reduced size of crystallites, which is characteristic of α-MnO 2 because of its tunnel-like structure and the potential inclusion of defects in the lattice or interstitial species. Conversely, the red diffraction pattern is associated with β-$MnO_2$ and matches the reference pattern of JCPDS card no. 24-0735, suggesting the tetragonal structure of rutile. The prominent diffraction peaks located at around 28.7°, 37.3°, 41.0°, 42.8°, 56.6°, and 59.4° are assigned to the (110), (101), (111), (210), (211), and (220) planes, respectively. These are sharper and more intense than those of the α-phase, indicating a greater extent of crystallinity and larger crystallite size. The small size of $MnO_6$ octahedra in β- $MnO_2$ helps in stabilizing its structure and its clear cut diffraction properties [15]. There is also the vertical stick pattern below the corresponding diffraction profile depicting standard positions of the peaks of the respective JCPDS cards which further confirms the identification of the phases. The fact that the experimental diffraction peaks are very close to the standard reference lines confirms the successful production of phase-pure α- and β-$MnO_2$. In general, this figure shows the different structural features of the two polymorphs, in which, α-$MnO_2$ has a less ordered tunnel structure, whereas β-$MnO_2$ has a highly crystalline and thermodynamically stable rutile-type phase.

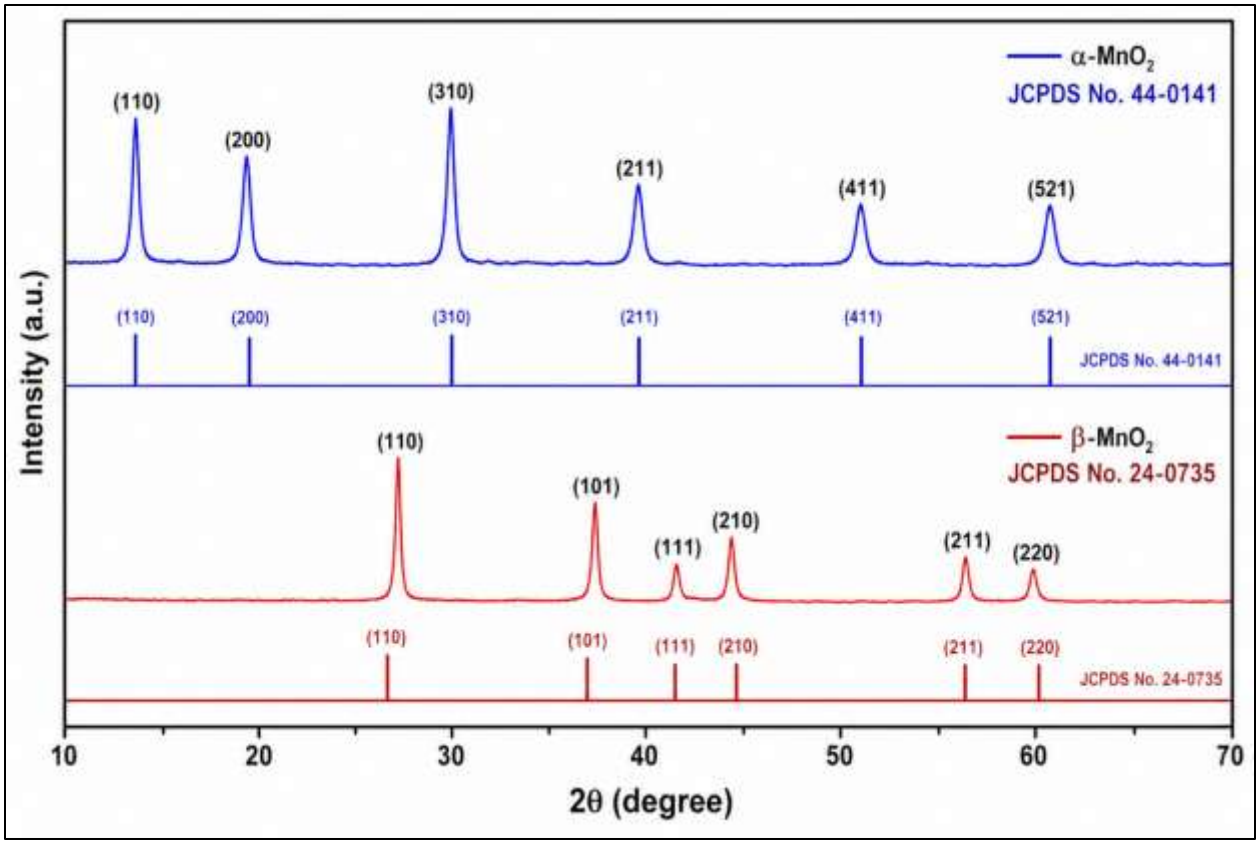


**Figure 2: XRD patterns of $MnO_2$ showing α-phase (blue, JCPDS No. 44-0141) and β-phase (red, JCPDS No. 24-0735); indexed peaks and reference stick patterns confirm the formation of tetragonal hollandite (α) and rutile-type (β) structures**.

### 2.2 SEM and EDS analysis

The scanning electron microscopy (SEM) and energy-dispersive X-ray spectroscopy (EDS) were used to analyze the surface morphology and the elemental composition of the synthesized $MnO_2$ nanostructures. In the SEM image of $MnO_2$ nanowires figure 3 (a), the image depicts dense network of elongated, wire-like, high aspect ratio structures randomly oriented and uniformly distributed on the surface. These nanowires create a porous structure that is interconnected, which is beneficial to increase the surface area and transport charges [16]. ]. Conversely, the figure 3 (b) in the supplementary material of SEM image of $MnO_2$ nanosheets has a layered, flake-like structure, comprising of thin sheets, arranged in a hierarchical manner. The nanosheets are loosely stacked and have irregular edges thus assume a flower-like shape which offers numerous active sites and better ion diffusion pathways [17]. ESD analysis further confirmed the elemental composition of the two morphologies. The EDS spectrum of $MnO_2$ nanowires (Figure 3) has powerful characteristic peaks of manganese (Mn) and oxygen (O), and it proves the successful construction of MnO 2. The fact that no further peaks are produced shows that the synthesized material is of high purity. Likewise, the EDS spectrum of $MnO_2$ nanosheets (Figure 4) also demonstrates distinctive Mn and O peaks without any traceable impurities, which also confirms the chemical composition. The differences in the relative weight and atomic percentages of the nanowires and the nanosheets can be ascribed to minor morphological, thickness, and surface exposure differences [18]. In general, the SEM and EDS findings affirm efficient preparation of high-quality $MnO_2$ with discrete nanowire and nanosheet structures both of which can be used in higher functional applications.

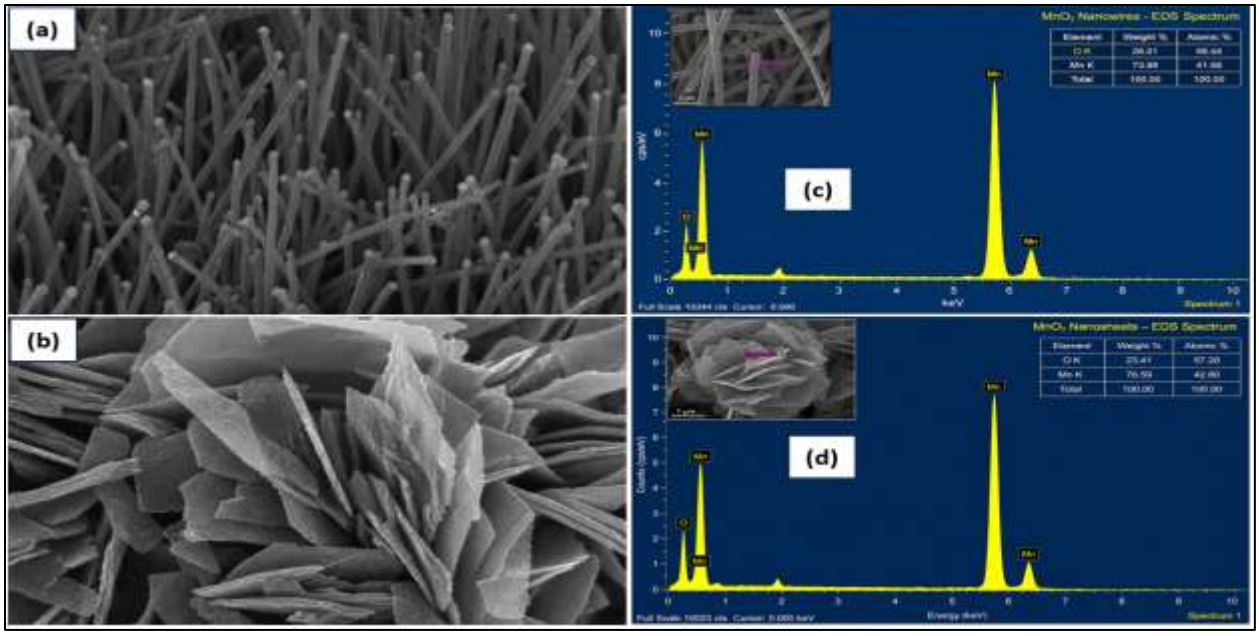


**Figure 3: SEM morphology of (a) α-$MnO_2$ (b) β-$MnO_2$ while (c) eds spectrum of α-$MnO_2$ and (d) β-$MnO_2$ respectively**

### 2.3 FTIR analysis

To examine the vibrational properties and verify the formation of manganese dioxide phases, the FTIR spectra of α-$MnO_2$ (blue line) and β -$MnO_2$ (red line) were taken in the wavenumber range of 4000-500 cm -1. A wide absorption band at around 3430 cm-1 can be seen in both spectra, which is associated with the OH stretch of the adsorbed water molecules, which means that there are surface hydroxyl groups. A less intense band at around ~1620 cm-1 is the H -O -H bend of molecular water, which once again confirms that moisture had been adsorbed on the sample surface. In the fingerprint area, there are clear bands that relate to the Mn-O bonding. The maximum of the absorption at approximately 1080 cm-1 is attributed to Mn-O stretching vibrations indicating the development of the metal-oxygen structure [19]. Moreover, bands in close proximity to $MnO_2$. The presence of a strong absorption below 600 cm -1, and especially near 500 cm -1, is associated with Mn-O lattice vibrations, and proves the crystalline structure of the oxide. Particularly, it is worth mentioning that the minor changes in the positions of the peaks and the differences in the magnitudes between the α-$MnO_2$ and β -$MnO_2$ imply that the crystal structures and the local bonding environments of these two materials are not the same. Such differences are due to the nature of the tunnel structures and geometry of coordination in the two polymorphs that affect the strength of MnO bond and the vibrational behavior. In general, the FTIR data confirms the efficient production of both α and β phases of $MnO_2$ and underlines their structural dissimilarity on a molecular level.

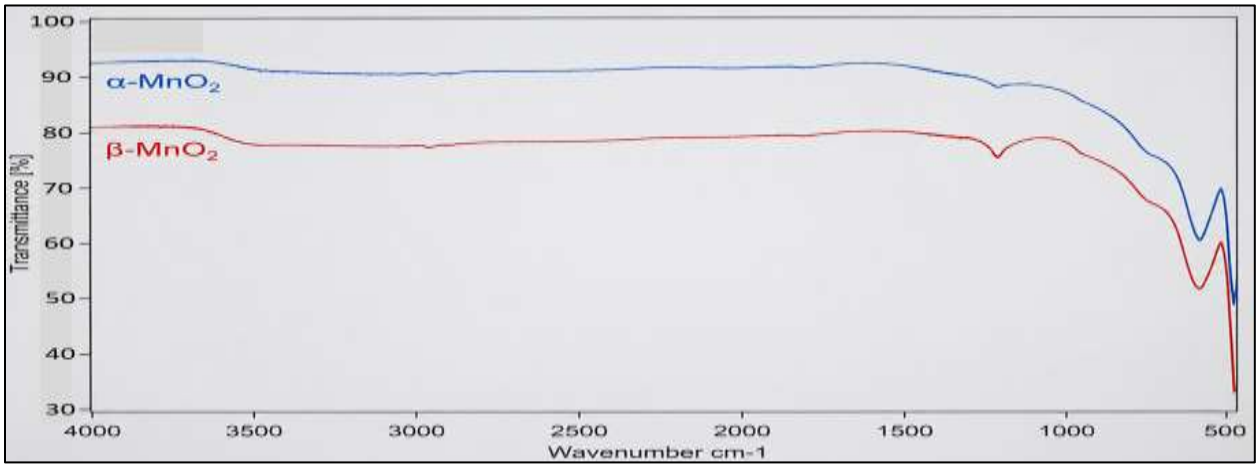


**Figure 4 : FTIR spectra of α-$MnO_2$ (blue) and β-$MnO_2$ (red) recorded in the range 4000–500 $cm^{-1}$, showing characteristic O–H vibrations of adsorbed water and Mn–O lattice vibrations, confirming the formation and structural differences of the two $MnO_2$ phases.**

### 2.4 UV-Vis, analysis

]. To analyze the optical behavior of α-$MnO_2$ and β -$MnO_2$, the UV -Vis, and absorption spectra of these compounds were recorded within the wavelength range (200-800 nm). The two samples have high absorption in the UV region that gradually decreases towards the visible region implying that they are semiconducting. The 360 nm absorption edge is relatively sharp in the β -$MnO_2$ and red-shifted in β -$MnO_2$ which indicates a higher absorption of visible light in the β phase at 430 nm [20]. This change may be explained by variations in crystal structure and electronic state, which determine light-harvesting efficiency of the materials. Tauc plots were also plotted to further assess the optical band gap by plotting $(\alpha h\nu)^{1/2}$ vs photon energy (hν) assuming an indirect allowed transition. The straight part of both curves was then extrapolated to meet the energy axis to give the values of the band gaps. The band gap of 3.13 eV is estimated to be the band gap of $MnO_2$ and 2.63 eV is the band gap of β -$MnO_2$. There is a lower band gap of β-$MnO_2$, which means that it has a better electronic conductivity and visible absorption than β -$MnO_2$. These findings indicate that structural differences between the 0 and 0 phases can have a substantial impact on the optical characteristics, with β -$MnO_2$ being a better choice when it comes to applications that require an efficient absorption of visible light, including photocatalysis and optoelectronics [21].

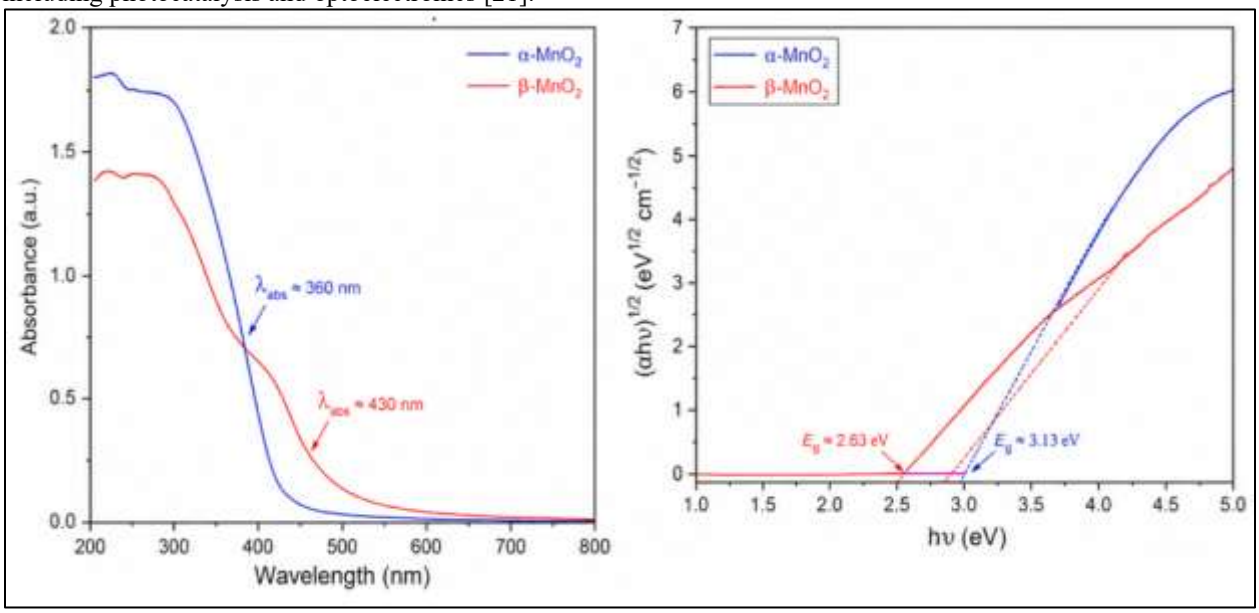


**Figure 5 : UV–Vis, absorption spectra and corresponding Tauc plots of α-$MnO_2$ (blue) and β-$MnO_2$ (red), showing absorption edges and estimated band gap energies, highlighting enhanced visible light absorption and lower band gap of β-$MnO_2$ compared to α-$MnO_2$.**

## 3. Biomedical application

### 3.1 Antibacterials properties

The figure illustrates the antibacterial performance of two polymorphs of manganese dioxide ($MnO_2$), namely α-$MnO_2$ (birnessite-type) and β-$MnO_2$ (pyrolusite-type), against representative Gram-negative (E. coli) and Gram-positive (S. aureus) bacterial strains. Both materials exhibit strong bactericidal activity, which is primarily attributed to their ability to generate reactive oxygen species (ROS) and induce oxidative stress in microbial cells [22]. In the case of α-$MnO_2$, the layered birnessite-type structure facilitates redox cycling between $Mn^{4+}$ and $Mn^{2+}$ states, promoting the formation of ROS such as superoxide radicals ($O_2^{\bullet-}$), hydroxyl radicals (•OH), and hydrogen peroxide ($H_2O_2$). These reactive species interact with bacterial cells, causing disruption of the cell membrane, increased permeability, and eventual leakage of intracellular components [23]. The schematic representation shows the transition from intact bacterial cells to damaged cells, highlighting membrane disintegration as a key antibacterial mechanism. This effect is further supported by the zone of inhibition images, where clear inhibition halos are observed around α-$MnO_2$-treated samples, in contrast to the dense bacterial growth seen in untreated controls. Quantitative bacterial viability analysis (CFU/mL) demonstrates a reduction of more than 99.9% in viable colonies for both E. coli and S. aureus, confirming the high antibacterial efficacy of α-$MnO_2$. Similarly, β-$MnO_2$, characterized by its more compact pyrolusite-type crystalline structure, also exhibits significant antibacterial activity through ROS-mediated pathways. Although its structural arrangement differs from α-$MnO_2$, it still supports redox reactions that generate oxidative species capable of damaging bacterial cells [24]. The figure shows comparable morphological changes in bacteria exposed to β-$MnO_2$, including membrane disruption and cytoplasmic leakage. The zone of inhibition assays again reveal pronounced antibacterial effects, with distinct clear zones surrounding β-$MnO_2$ disks, indicating effective suppression of bacterial growth [25]. The corresponding CFU analysis further confirms a substantial decline in bacterial viability, exceeding 99.9%

reduction for both tested strains. Overall, the figure demonstrates that both α-$MnO_2$ and β-$MnO_2$ possess potent broad-spectrum antibacterial activity against Gram-negative and Gram-positive bacteria. Their bactericidal action is predominantly governed by ROS generation and oxidative stress, which compromise bacterial cell integrity and inhibit survival. While both polymorphs are highly effective, subtle differences in their crystal structures may influence the efficiency of ROS production and, consequently, their antibacterial performance. These findings highlight the potential of $MnO_2$-based nanomaterials as promising antimicrobial agents for biomedical and environmental applications [26].

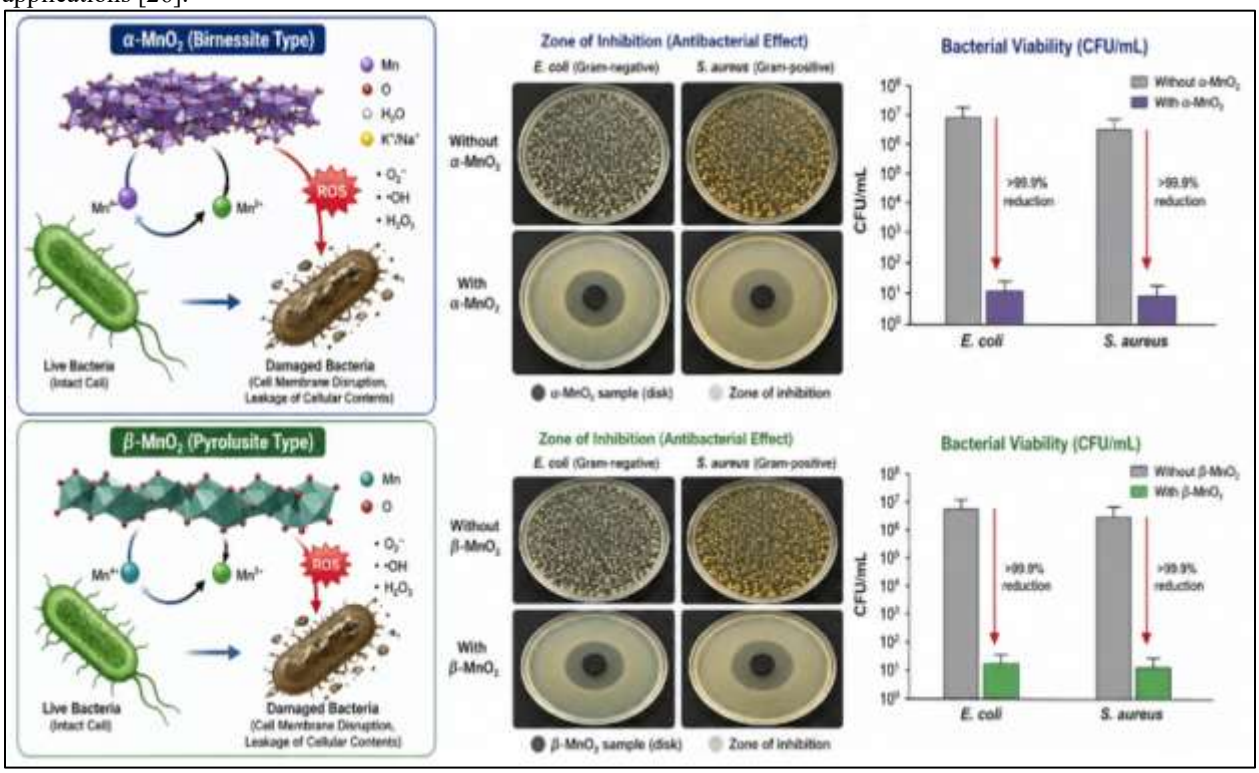


**Figure 6 : Antibacterial activity of β-$MnO_2$ nanosheets compared to α-$MnO_2$ nanowires.**

### 3.2 Antifungal properties

Antifungal action of manganese dioxide ($MnO_2$ ) has various polymorphic forms, predominantly α-$MnO_2$ and β-$MnO_2$, and their activity can differ considerably depending on the crystal structure, surface characteristics and redox behavior[27]. Overall, both types show antifungal properties, but α-$MnO_2$ is usually more active than β-$MnO_2$, which can be explained by the fact that the former has a tunneled crystal structure that offers a greater surface area and more active sites that can interact with fungal cells. The antifungal activity of $MnO_2$ is mainly linked to the production of reactive oxygen species (ROS) and impairment of fungal cell integrity. Exposing fungal cells to $MnO_2$ nanoparticles causes the onset of oxidative stress by the production of ROS, including superoxide radicals and hydrogen peroxide [28]. These reactive species destroy key cellular components such as lipids, proteins and nucleic acids, eventually resulting in disrupted cell metabolism and cell death. Also, $MnO_2$ particles may react directly with fungal cell wall and membrane leading to structural deformation, increased permeability and leakage of intracellular contents. In α-$MnO_2$, defects are more densely distributed and tunnels are bigger and therefore, promote improved ion exchange and ROS formation, which is why it is more effective as antifungal[29]. The polymorph is also more likely to be dispersed in the biological media, enhancing its chances to get into contact with fungal cells. Conversely, β-$MnO_2$ is smaller and more stable with a rutile-like structure and hence fewer active sites on its surface and relatively lower reactivity, thus, lower antifungal activity. Generally, experimental studies reveal that both α- and β -$MnO_2$ have dose-dependent antifungal effects against typical fungal strains (i.e. Candida albicans and Aspergillus niger) with β -$MnO_2$ consistently generating larger inhibitory zones and lower minimum inhibitory concentrations (MICs). This disparity emphasizes the role of crystal phase engineering in streamlining $MnO_2$-based nanomaterials in the biomedical antifungal application[30]. On balance, the superior antifungal activity of α-$MnO_2$ over β-$MnO_2$ is largely determined by its structural benefits, increased surface reactivity, and greater ROS-mediated oxidative stress generation, thus it is a better antifungal candidate nanomaterial.

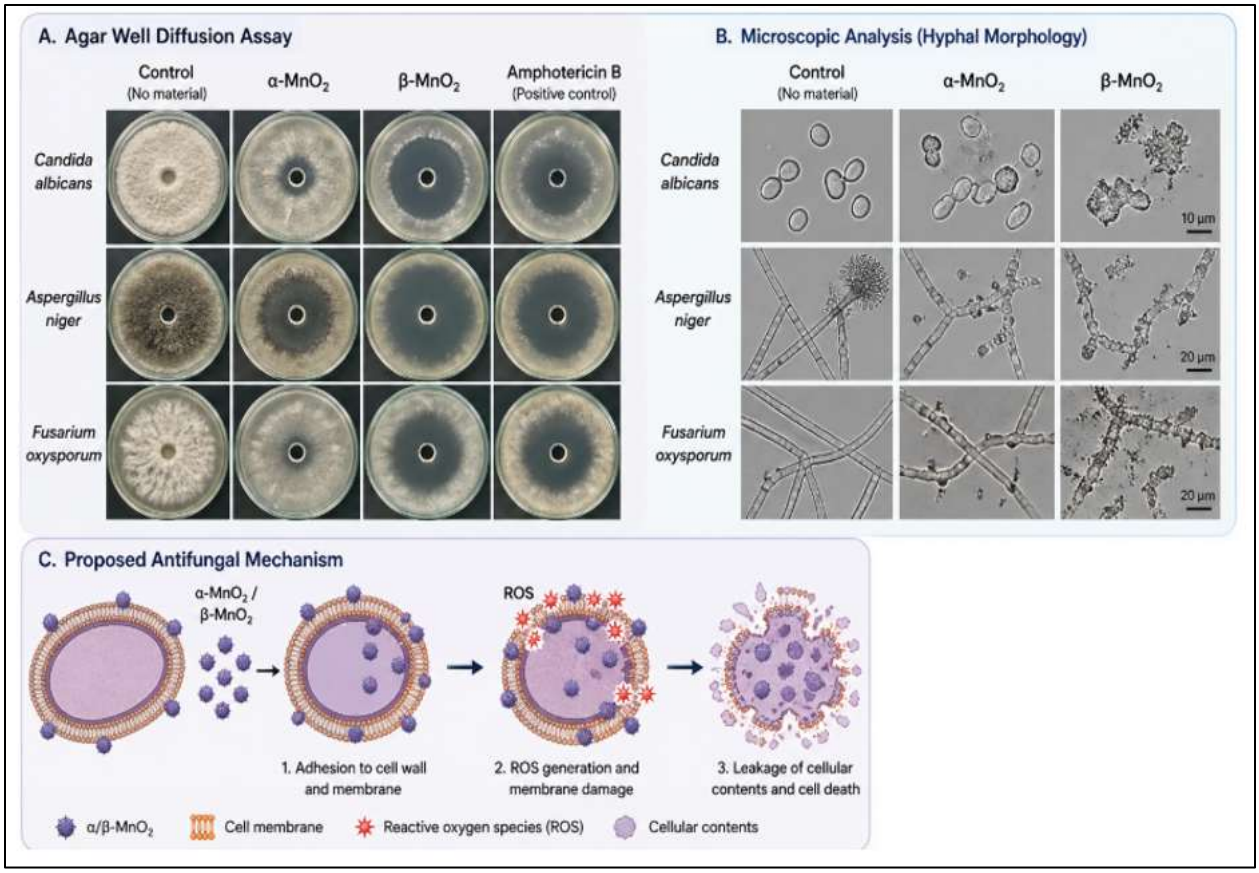


**Figure 7: Antifungal activity of β-$MnO_2$ nanosheets compared to α-$MnO_2$ nanowires.**

## CONCLUSION

The research work shows a straightforward and environmentally friendly green synthesis plan of the effective production of α- and β-$MnO_2$ nanostructures with different morphologies and phase dependent characteristics. Detailed characterization ascertained that α-$MnO_2$ and β-$MnO_2$ developed nanowire and nanosheet morphologies respectively with high purity and distinct crystalline phases. Compared to the two materials, β-$MnO_2$ showed a better antibacterial and antifungal property, which can be attributed to its high surface area and good nanosheet structure that facilitates more contact with the membrane of the microbes. These results indicate that $MnO_2$ structural, optical and biological properties can be successfully tune by phase engineering using green synthesis. The enhanced antimicrobial activity of β-$MnO_2$ underlines its adaptation as a promising compound in the biomedical field such as antimicrobial coatings and therapeutics. This research does not only give an insight into morphology-controlled synthesis of $MnO_2$ but also lays a sustainable avenue to the creation of functional nanomaterials to be used in biomedical applications.

## REFERENCES

1. Ahmad, K., et al., Enhanced supercapacitor performance of copper-doped NiO nanostructures synthesized via hydrothermal method. 2025: p. 113060.
2. Khan, A., et al., Modeling and Performance Analysis of PM6: Y6 Based Inverted Bulk Heterojunction Organic Solar Cells through SCAPS-1D Simulation. 2026. **14**(1): p. 384-399.
3. Du, T., et al., Antibacterial activity of manganese dioxide nanosheets by ROS-mediated pathways and destroying membrane integrity. 2020. **10**(8): p. 1545.
4. Wang, L., et al., Antimicrobial activity of silver loaded MnO2 nanomaterials with different crystal phases against Escherichia coli. 2016. **41**: p. 112-120.
5. Liang, Z., et al., Oxygen-defective MnO2/ZIF-8 nanorods with enhanced antibacterial activity under solar light. 2022. **428**: p. 131349.
6. Lu, Y., et al., Wound-healing material with antibacterial and antioxidant functions, constructed using keratin, hyperbranched polymers, and MnO2. 2023. **15**(25): p. 29841-29853.
7. Yan, Y., et al., Enhanced spontaneous antibacterial activity of δ-MnO2 by alkali metals doping. 2022. **9**: p. 788574.
8. Zou, Y., et al., Ultrafast Charged MnO2 Nanosheets/Carbon Fiber with Mechanical and Postcharging Antibacterial Activity. 2025. **25**(12): p. 4751-4758.

9. Wang, S., et al., Injectable redox and light responsive MnO2 hybrid hydrogel for simultaneous melanoma therapy and multidrug-resistant bacteria-infected wound healing. 2020. **260**: p. 120314.
10. Ogunyemi, S.O., et al., The bio-synthesis of three metal oxide nanoparticles (ZnO, MnO2, and MgO) and their antibacterial activity against the bacterial leaf blight pathogen. 2020. **11**: p. 588326.
11. Ikram, M., et al., Carbohydrate polymers based MnO2 nanostructures for catalytic and antibacterial activity; kinetic modeling and molecular docking analysis. 2024. **181**: p. 108633.
12. Alimohammadi, F., et al., Antimicrobial properties of 2D MnO2 and MoS2 nanomaterials vertically aligned on graphene materials and Ti3C2 MXene. 2018. **34**(24): p. 7192-7200.
13. Fitriannisa, I., et al., Unveiling the Antibacterial Efficacy and Mechanistic Insights of MnO2 Nanoparticles for Advanced Therapeutic Applications. 2025. **26**(18): p. 9104.
14. Wang, X., et al., Rapid and highly effective noninvasive disinfection by hybrid Ag/CS@ MnO2 nanosheets using near-infrared light. 2019. **11**(16): p. 15014-15027.
15. Wu, B., et al., The enhanced photocatalytic properties of MnO2/g-C3N4 heterostructure for rapid sterilization under visible light. 2019. **377**: p. 227-236.
16. Arumugam, B., et al., Synthesis of MnO2 decorated mesoporous carbon nanocomposite for electrocatalytic detection of antifungal drug. 2022. **182**: p. 107891.
17. Lu, H., et al., Biogenic synthesis of MnO2 nanoparticles with leaf extract of Viola betonicifolia for enhanced antioxidant, antimicrobial, cytotoxic, and biocompatible applications. 2021. **12**: p. 761084.
18. Bonab, H.R., A.A. Matin, and M.J.J.o.C.B. Soylak, Hierarchical C-Fe2O3@ MnO2 nanostructured sorbent; application in dispersive-μ-solid phase extraction of antifungal drugs. 2025: p. 124858.
19. Faisal, S., et al., Fagonia cretica-mediated synthesis of manganese oxide (MnO2) nanomaterials their characterization and evaluation of their bio-catalytic and enzyme inhibition potential for maintaining flavor and texture in apples. 2022. **12**(5): p. 558.
20. Bano, L., et al., Green synthesized MnO2 nanoparticles: evaluation of synthesis methodologies and broad-spectrum therapeutic potential. 2026: p. 1-30.
21. Shah, F., et al., Fagonia cretica-Mediated Synthesis of Manganese Oxide (MnO2) Nanomaterials Their Characterization and Evaluation of Their Bio-Catalytic and Enzyme Inhibition Potential for Maintaining Flavor and Texture in Apples. 2022. **12**(5): p. 558.
22. Morbale, S.T., S.D.J.N. Patil, and Nanotechnology-Asia, Green synthesis of MnO2 NPs using Blumea lacera leaf extract and its antimicrobial study. 2022. **12**(2): p. 74-83.
23. Chaudhary, P., et al., Transforming Citrus sinensis Seed Waste Into Modified MnO2 Nanoparticles as Photocatalytic and Biological Agent. 2026. **11**(9): p. e03865.
24. Elharrif, M.G., N.A. Hassan, and M.J.И.и.и. Sharaf, Biosynthesis of novel MnO2 nanocapsules via c. spinosa extract and honeybee-derived chitosan: exploring antibacterial and anticancer properties. 2024. **14**(5): p. 1002-1016.
25. Anguraj, G., et al., MnO2 doped with Ag nanoparticles and their applications in antimicrobial and photocatalytic reactions. 2023. **13**(2): p. 397.
26. Warsi, M.F., et al., Copper and silver substituted MnO2 nanostructures with superior photocatalytic and antimicrobial activity. 2022. **48**(4): p. 4930-4939.
27. Akhtar, M., et al. Facile Synthesis of MnO2 Nanoparticles and Gauging Their Latency as Nanocosmetics. in International Conference on Emerging Materials, Smart Manufacturing and Computational Intelligence. 2024. Springer.
28. Sabeha, S., Z.J.J.I.A.-H.J.F.P. Shanan, and A. Sciences, Synthesis of manganese dioxide nanoparticles by plant extract mediated and their effect on biofilm formation. 2023. **36**(3): p. 91-99.
29. Maruthapandi, M., et al., Nanoengineered γ MnO2 Accelerates the Degradation of Antibiotic-Resistant Biofilms. 2026. **16**(3): p. 367.
30. Shkir, M.J.T.E.P.J.P., An eco-friendly Chlorophytum borivilianum plant extract-mediated green synthesis of β-MnO2 NPs and their applications as remarkable photocatalyst and antibacterial agents. 2025. **140**(7): p. 631.